Available online at www.sciencedirect.com

jmr&t Journal of Materials Research and Technology

journal homepage: www.elsevier.com/locate/jmrt

Original Article

Effect of focal position offset on joint integrity of AA1050 battery busbar assembly during remote laser welding

Tianzhu Sun[*], *Pasquale Franciosa*, *Dariusz Ceglarek*

Warwick Manufacturing Group (WMG), University of Warwick, Coventry, CV4 7AL, UK

ARTICLE INFO

Article history:
Received 14 December 2020
Accepted 2 August 2021
Available online 9 August 2021

Keywords:
Remote laser welding (RLW)
Battery busbar assembly
AA1050
Joint integrity
Focal position offset

ABSTRACT

This paper aims at studying the impact of focal position offset on joint integrity of AA1050 battery busbar during remote laser welding. Welding experiments were conducted at different focal position offsets in the AA1050 L-joint with the integration of laser beam oscillation. The impact of focal position offset was evaluated by multiple joint indicators including weld geometry, thermal profile, weld porosity and mechanical strength. Results showed that defocusing of the laser beam tends to be favourable for the reduction of peak temperatures and weld porosity. However, a defocusing more than 3 mm can lead to 60% drop in bonding integrity and 40% loss of joint strength. A tolerance window of [-2 1] mm was determined for the focal position offset, corresponding to 70% and 30% of the Rayleigh length. This result is a useful reference to inform precise focal position control with respect to the accumulated variations of part tolerance, part-to-part gap and part positioning errors. This study also indicated that the thermal measurement can be a potential approach for in-process monitoring of joint integrity. Indeed, the peak temperature near the weld zone showed good linear correlation with off-line detectable joint indicators including weld depth, weld width at interface, weld tensile strength and weld porosity.

1. Introduction

Battery pack is the core sub-system of Battery Electric Vehicles (BEVs). Recent advances in large-capacity battery packs with increased energy density have enabled a longer driving range and overall better driving performance, which has greatly expanded the market for BEVs [1,2]. Using multiple types of busbars provides robust mechanical and electrical connections of battery cells against external disturbances such as vibration of vehicle during service and thermal loading due to charging and discharging of the battery itself [3]. Fig. 1 shows a representative view of the busbar configuration in a battery module consisting of flat top busbar and side busbar [4]. Nowadays, aluminium alloys, in particular 1xxx series, tend to be the preferred material for busbar components due to their competitive properties and costs compared to copper. For instance, aluminium busbars have shown weight reduction by 50% and cost saving by up to 20% compared to copper busbars [5].

* Corresponding author.
E-mail address: Tianzhu.sun@warwick.ac.uk (T. Sun).

https://doi.org/10.1016/j.jmrt.2021.08.002

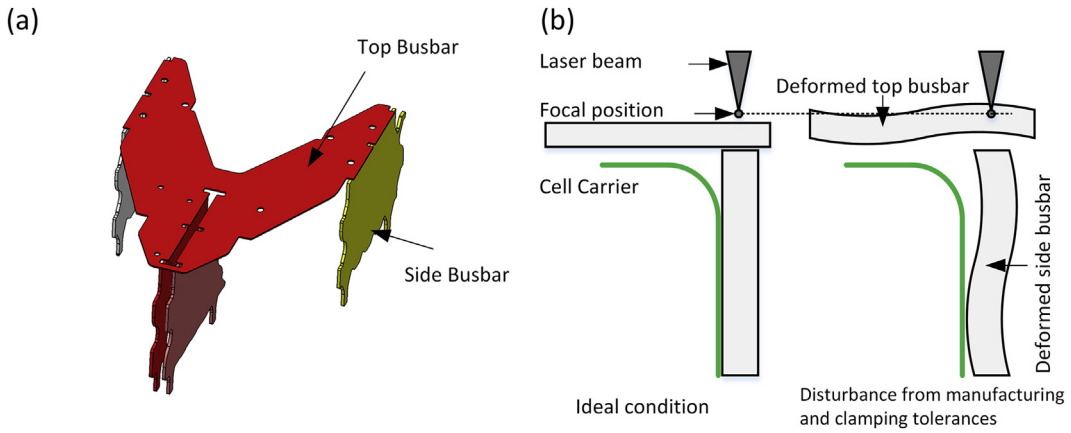

Fig. 1 – Schematic diagrams showing (a) aluminium battery busbar in BEV battery module for the connection of battery cells [35] and (b) laser beam positioning error due to the manufacturing and clamping tolerances of aluminium busbar sheets.

With regards to welding technology, there is a growing interest in applying Remote Laser Welding (RLW) in battery manufacturing due to several advantages such as single-sided and non-contact access, reduced as well as controlled heat input, along with high-speed welding process [6,7]. As the variation in shape and geometry of the welds generates unequal electrical resistances within the same battery pack which further results in the uneven current loads and inhomogeneous cell degradation, a stable welding process is therefore, necessary.

Joint integrity is defined by multiple joint indicators, as indicated in international standards [8]. The focus of this paper will be on weld porosity, weld depth and interface width (all directly correlated to structural and electrical integrity), and thermal distribution. Thermal distribution during the welding process plays a crucial role in avoiding damage to the adjacent components (i.e., battery cells, insulators, etc.) [9]. Recently, several techniques have been proposed to control weld porosity [10]. For example, Jiang et al. [11] reported that low vacuum welding at up to 0.1 kPa effectively promotes the escape of gas bubbles by upward fluid flow in the rear of weld pool, which is driven by the suppression of plasma plume and reduction in boiling point. Haboudou et al. [12] proposed that the use of dual spot beam can lead to a reduction in weld porosity by extending the laser–material interaction time and stabilizing the keyhole. AlShaer et al. [13] showed a significant elimination of weld porosity by short pulse laser surface cleaning prior to laser welding process because of the removal of contaminations and oxide layers. More recently, Wang et al. [14] reported that laser beam oscillation allows to reduce the weld porosity as the mechanically stirring effect from oscillated beam facilitates the material flow and stabilizes the keyhole. In addition, an enhanced joint strength was observed by the utilisation of beam oscillation due to a significantly wider weld zone [15]. However, it should be noted that in the application of busbar assembly the amplitude of beam oscillation is greatly limited by the thickness of side busbar as shown in Fig. 1 and the resultant effect on the distribution of weld porosity is still unclear.

Motivated by the fact that variations in laser beam positioning resulting from the manufacturing and clamping tolerances of thin sheets (Fig. 1(b)) can generate an accumulated deviation of more than 1 mm [8] and therefore, lead to the loss of functional properties (both structural and electrical integrity), this paper aims at experimentally evaluating the impact of focal position offset on joint integrity. Top and side busbars were made of AA1050 sheets and welded in the overlap L-joint configuration. Weld porosity, weld depth and interface width were investigated by optical microscope and X-ray computed tomography (CT). Thermal history during welding process was recorded by infrared thermal camera. Tensile peel test and micro-hardness test were carried out for the characterisation of mechanical performance.

2. Experimental details

2.1. *Welding procedure*

A 6 kW diode laser (LaserLine GmbH, Germany), with a beam parameter product of 6 mm mrad was used. The laser beam was delivered through an optical fibre of 150 μm diameter and coupled with the WeldMaster remote welding head (Precitec GmbH, Germany), which comes with 150 mm collimating length and focal length of 300 mm. The resulting Rayleigh length (Z_R) is 2.8 mm. No shielding gas nor filler wire was used throughout the experiments.

The materials used in this paper were 1.5 mm thick AA1050-H111 (top busbar) and 2 mm thick AA1050-H14 (side busbar) sheets, having a nominal composition of <0.4% Fe, <0.25% Si, <0.07% Zn, <0.05% Mg, <0.05% Cu, <0.05% Mn and balance Al. Sheets were machined into 38 mm × 120 mm coupons and wiped with acetone before welding to remove surface contaminations. Welding was carried out in an overlap L-joint configuration at a nominal 0 mm part-to-part gap and zero incident beam angle as shown in Fig. 2. The reference point in Fig. 2 (a) was theoretically aligned to the mid-thickness of the side busbar before welding. A sine oscillation path with an amplitude of 0.3 mm (Fig. 2 (b)) was employed throughout all welding trials. Laser beam focal position was calibrated with the triangular prism block supplied by Precitec (Fig. 2 (c)). The study was carried out in two

consecutive steps (I) pre-selection of beam oscillation frequency; and, (II) study of focal position offset with the fixed oscillation frequency obtained in step (I). Detailed welding parameters of both steps are listed in Table 1. The specific point energy density (*SPED*) at the surface of top busbar is defined as the input energy over each point along the laser beam path [16], normalised over the area of the laser spot, and expressed in Eq. (1)

$$SPED = \frac{4P \cdot I_m}{\pi d_{A_Z}^2} \quad (1)$$

where d_{A_Z} is the diameter of laser spot at focal offset A_Z, given by Eq. (2) and I_m is the averaged laser-to-material interaction time over one oscillation cycle expressed in Eq. (3).

$$d_{A_Z} = d_0\sqrt{1+\left(\frac{A_Z}{Z_R}\right)^2} \quad (2)$$

$$I_m = \frac{d_{A_Z}}{v_m} \quad (3)$$

where $d_0 = 0.268$ mm is the laser spot diameter at focus and v_m is the mean velocity of laser beam over one oscillation cycle expressed in Eq. (4), and calculated at 4 points, A ($t = 0$), B ($t = 1/(4f)$), C ($t = 1/(2f)$), and D ($t = 3/(4f)$). S_y is the velocity in the transverse y direction and given by $S_y(t) = 2\pi A_y f \sin(2\pi f t)$, where t is the time.

$$v_m = \frac{1}{4}\sum_{t=0,\frac{1}{4f},\frac{1}{2f},\frac{3}{4f}}\sqrt{S_x^2 + S_y^2(t)} \quad (4)$$

Combining Eqs (2)–(4) into Eq. (1) leads to a synthetic index which accounts for travel speed (S_x), input power (P), beam focal position offset (A_Z), beam oscillation amplitude (A_y) and frequency (f).

2.2. Thermal measurement

According to industrial recommendations, the battery cell and cell carrier are commonly located at a few millimetres beneath the top busbar [17] as conceptually shown in Fig. 2(a). This raises the need for temperature control in order to avoid damage to the battery cell and cell carrier during the laser welding process. Thermocouples were disregarded since they normally have the spatial resolution of 0.5–1 mm depending upon the size of thermocouple itself and the positioning of measuring probe is an inaccurate task which needs to be repeated for each weld. Therefore, in order to cover the full field view of the weld and extract temperatures at multiple positions relative to the weld zone, a FLIR® A655sc IR camera was used in this paper. The camera was mounted on the ball-head clamp, which is perpendicular to the surface of side busbar at a standing-off distance of 650 mm as shown in Fig. 3. The IR sensor has a resolution of 640 × 480 pixels and can collect data at a frequency of 50 Hz. Side busbar were covered by 0.2 mm thick Scotch® Vinyl electrical tape to eliminate multi-reflections from aluminium surface and FORMEX™ GK insulator was placed behind the side busbar to avoid heat sinking. The tape has an emissivity of 0.96 and was calibrated by pre-screening trials with thermocouples. A temperature measurement channel of −15 to 150 °C was selected as a trade-off between the image contrast quality and working temperature of the electrical tape (limited to 200 °C). Thermal history was extracted from thermal images at different distances beneath the weld top surface, D_W ranging from 5 to 10 mm along three vertical probe lines (near weld start, in the middle and near weld end, respectively, Fig. 3 (c)) for the understanding of thermal distribution near battery cell in response to the change of welding parameters.

2.3. Macro and micro weld zone characterization

Effective weld depth (D_E) and weld width at interface (W_E), as illustrated in Fig. 4(a), are used as key geometrical features in this paper to evaluate the bonding integrity between top busbar and side busbar. Under optical microscope (OM), D_E was measured from the top surface of side busbar to the root of fusion zone and W_E were given by the accumulated width of the intersection between fusion and top surface of side busbar. Acceptance limits on D_E and W_E (D_E greater than 25% of side busbar thickness and W_E greater than the 1.0 mm) have been adapted from international standards [8] to guarantee the minimum interface between the two busbars. In addition,

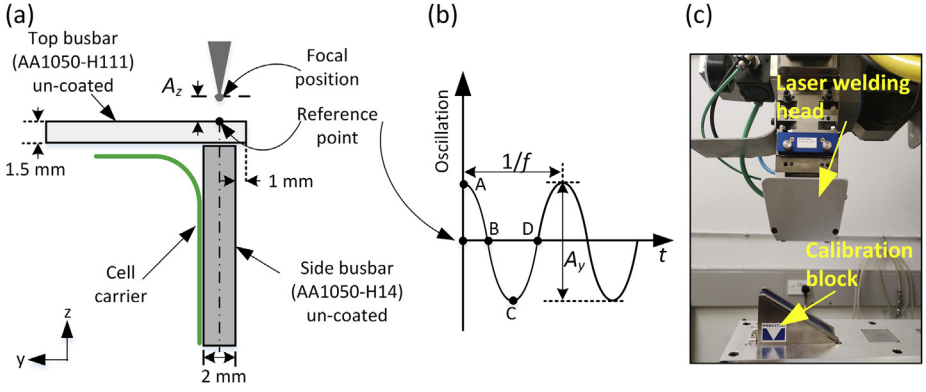

Fig. 2 – Schematic definition of overlap L-joint configuration for battery busbar assembly: (a) Front view and (b) representation of beam oscillation; and, (c) experimental set-up for laser beam focal position calibration with triangular prism block supplied by Precitec.

Table 1 – Matrix of welding parameters used in this paper.

Step (I): Pre-selection of beam oscillation frequency			
Laser Beam Power, P (kW)	2.0	Oscillation frequency, f (Hz)	50; 150; 200; 300
Welding speed, S_x (m/min)	4.0	Focal position, A_z (mm)	−2.5
Oscillation amplitude, A_y (mm)	0.3	Specific point energy density (J/mm^2)	95; 66; 57; 45
Step (II): Study of focal position offset			
Laser Beam Power, P (kW)	2.0	Oscillation frequency, f (Hz)	200
Welding speed, S_x (m/min)	4.0	Oscillation amplitude, A_y (mm)	0.3
Focal position, A_z (mm)	−4.0; −3.0; −2.5; −2.0; −1.0; 0; 1.0; 2.0; 2.5; 3.0; 4.0		
Specific point energy density (J/mm^2)	45; 51; 57; 64; 73; 76; 73; 64; 57; 51; 45		

depth of the fusion zone (D_F) and weld width at the top surface (W_T), depicted in Fig. 4(b) were used for the calculation of weld aspect ratio, expressed by W_T/D_F. Samples were prepared by metallographic polishing to 0.25 μm finish, followed by etching in sodium hydroxide (NaOH) solution for 2 mins. Automated micro-hardness mapping was performed using a Buehler Wilson® VH3300 Vickers hardness tester with an applied load of 0.1 kg for 10 s and 0.25 mm spacing between indents.

To provide a better visualization and precise analysis of weld porosity, X-ray CT was performed on the integrated weld in North Star Imaging® 3D X-ray CT inspection system. A voxel size of 0.015 mm was used among all measurements. 3D reconstruction of weld pores was carried out over a segment of 16 mm positioned symmetrically to the mid-length of the weld, to avoid disturbance from unstable processing parameters near weld start/end. 2D Raw images were first converted to binary images and any pixel referring to zero (black) within weld zone was regarded as pore and extracted for the subsequent spatial reconstruction. Two identical welds for each welding parameter were tested and the total volume of pores over unit weld length (1 mm) was

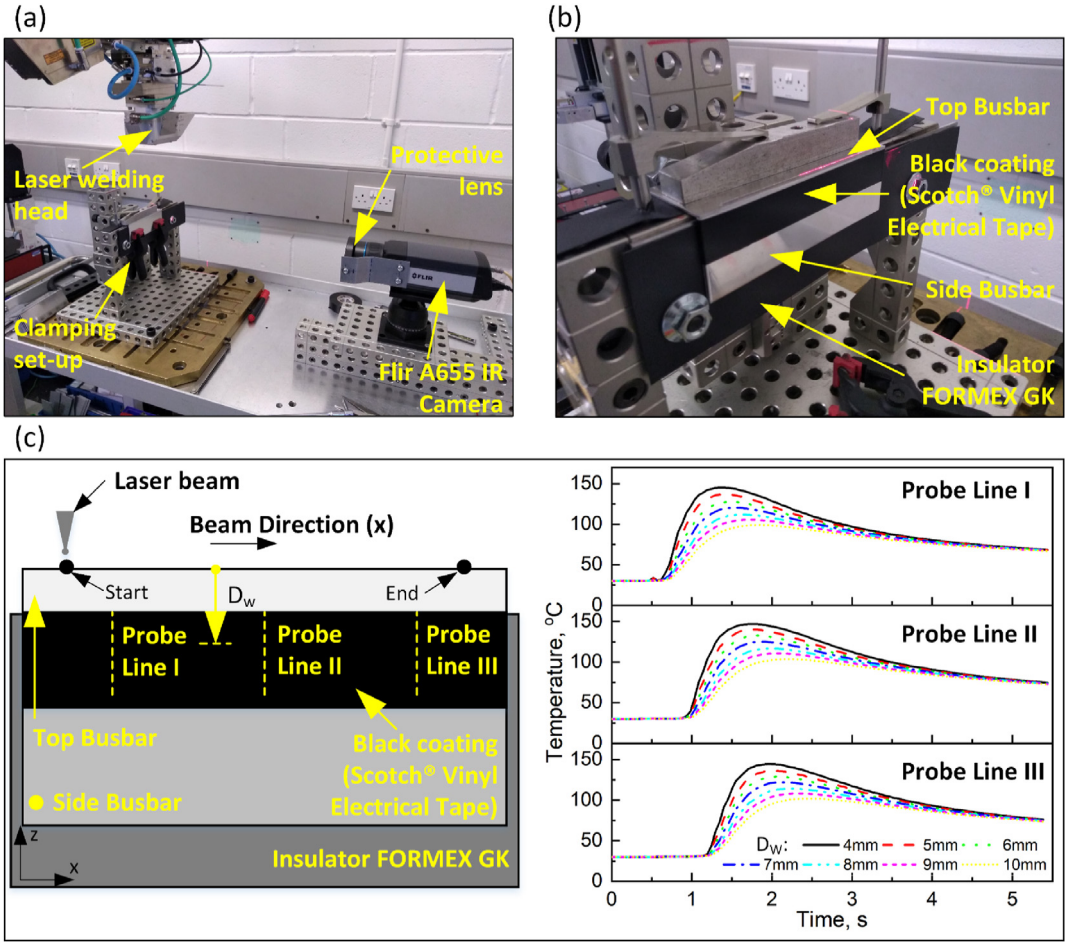

Fig. 3 – Experimental set-up for thermal measurement (a) overview, (b) detailed view and (c) representative thermal profiles at different depths.

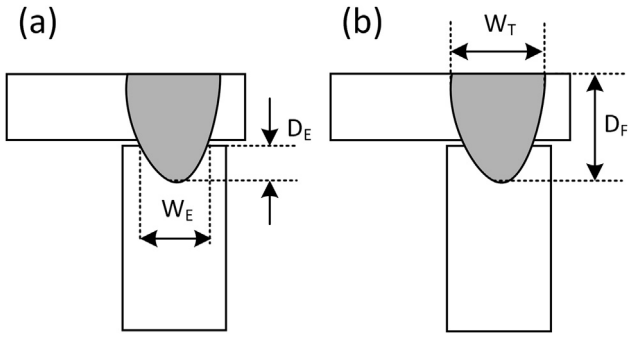

Fig. 4 – Key geometrical features of RLW L-joint (a) effective weld depth (D_E) and weld width at interface (W_E) for the evaluation of bonding integrity; and (b) depth of fusion zone (D_F) weld width at top surface (W_T) for the calculation of weld aspect ratio (W_T/D_F).

then calculated which allows 32 replications in total to show the deviation.

2.4. *Mechanical characterization*

In order to validate the mechanical requirement, tensile peel tests were performed using Instron 5985 Universal Testing System following ISO 6892–1:2016 tensile test standard [18]. Tensile peel loading was applied along the side busbar at a constant extension rate of 2 mm/min and the maximum loading was then extracted from the load-extension curve.

3. Results and discussion

3.1. *Step (I) - Pre-selection of beam oscillation frequency*

Fig. 5 shows representative 3D reconstruction of pores in welds produced at different beam oscillation frequencies. Pores can be mainly categorised into large pores at the weld root in the side busbar and small pores in the top busbar. Both types of pores uniformly distribute along the welding direction. Quantitative analysis of weld porosity as function of beam oscillation frequency is shown in Fig. 6 (a) and (b). The total volume of pores shows an increasing trend with frequency raising from 50 Hz to 200 Hz while a drop is determined with further increase in frequency from 200 Hz to 300 Hz, which can be visualized as inverse V-model of pores distribution with peak at 200 Hz.

This change in monotonicity is due to the simultaneous impact of thermal (dominant at the left of the inverse 'V') and mechanical (dominant at the right side of the inverse 'V') effects. The increasing beam oscillation frequency leads to a lower temperature in the weld zone (Fig. 6 (b)), as a result of the reduced specific point energy density and the keyhole therefore tends to be slimmer and less uniform, which is confirmed by a direct online X-ray imaging study reported by Fetzer et al. [19]. This results in a more unstable process and more frequent bubble formation in the molten pool. On the other hand, the mechanical stirring effect is stronger due to increasing frequency which, in turn, facilitates the melt flow and assists the bubbles to escape. Therefore, a drop in total volumes of pores was determined when oscillation frequency further increases from 200 Hz to 300 Hz. Fig. 6 (b) shows the change in volumes of pores along weld depth and reveals that pores from the interface between two busbars to the bottom of fusion zone in the side busbar are the dominant sources of weld porosity in this study.

It should be noted that the effect of oscillation frequency on the distribution of pores observed in this paper as inverse 'V' shape is in contradiction with research developed by Zhang et al. [20], which focused on laser welding of Al–6Mg in bead-on-plate configuration produced by an oscillated beam in circular path with amplitude of up to 4 mm and frequency ranging from 100 Hz to 800 Hz. They concluded that the total volume of pores is a monotonically decreasing function of beam oscillation frequency. This can be attributed to three phenomena. First, a sine oscillation path was used in our research, differentiating from the circular path which dramatically alter the melt flow and keyhole stability by the re-melting during the second half cycle. Secondly, the significant reduction of Mg content in 1050 aluminium alloy, compared with Al–6Mg alloy, greatly reduces the recoil pressure on the rear wall of keyhole and changes the dynamic behaviour of keyhole collapse [21]. Lastly, perhaps most importantly, the amplitude of beam oscillation employed in this paper was only 0.3 mm as it was limited by the thickness of side busbar, the mechanical stirring effect at low frequency is less efficient for the bubbles to escape.

One-way ANOVA with the significance level of 0.05 has showed p-value of ~0.016 for the test between beam oscillation frequency and total volumes of pores. This result statistically confirms that the variation of total volumes of pores is significant. Therefore, in step (II) of the experimentation an oscillation frequency of 200 Hz was employed in order to study the impact of the focal position offset under the most severe conditions (i.e., 200 Hz generates the highest level of porosity).

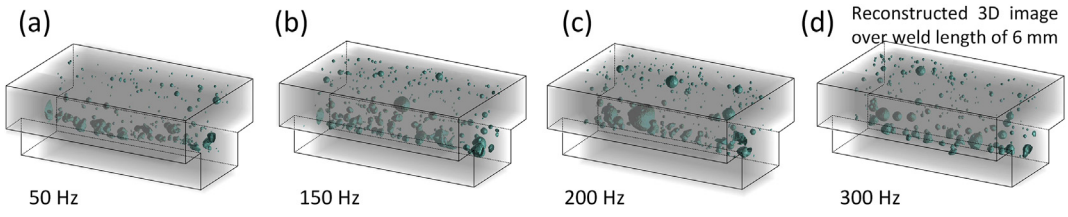

Fig. 5 – Representative 3D reconstruction of pores in welds produced with beam oscillation at (a) 50 Hz; (b) 150 Hz; (c) 200 Hz; and, (d) 300 Hz. Note that for a better visualisation, porosity over a weld length of 6 mm was displayed.

3.2. *Step (II) - Effect of focal position offset on power density and weld temperature*

In remote laser welding, effective heat input is related to the power dissipated into the workpiece and for a fixed power output, the power density is determined by the area of the laser spot intersecting the workpiece. Fig. 7 (a) reports the distribution of laser beam spot size and resultant input power density as function of focal position offsets. Results show that both positive and negative defocusing can lead to an increase in beam size and hence, a drop of input power density. Peak temperatures at the distance of 5–10 mm from the top surface with different focal positions in Fig. 7 (b) show that vertical diversion of laser beam can lead to a drop in peak temperature due to the reduction in power density. It also reveals that though negative defocusing causes shift of laser beam towards the battery cell, there is less thermal risk since the reduction of power density tends to be the dominating factor in this situation. In addition, an asymmetrical distribution of peak temperature has been determined and a negative defocusing generated a higher level of thermal field compared to positive defocusing at the same diversion level. This can be attributed to the fact, as proposed by Li et al. [22], that the up-flowing metal and back-flowing spatter can accumulate and stir the rear of molten pool for the case of positive defocusing, and result in a high heat-transferring efficiency on the molten pool surface. In comparison, this effect becomes less significant when the focal position moves deeper into the molten pool, which will stabilize the molten pool surface and retain more heat within the molten pool.

3.3. *Step (II) - Effect of focal position offset on weld shape and distribution of micro pores*

Fig. 8 plots the evolution of effective weld depth (D_E) and weld width at interface (W_E) as function of beam focal position offsets. It should be noted that a part-to-part gap of less than 0.12 mm was observed which, however, is within the range of 10% of the thickness of top busbar and has limited influence on weld geometry and porosity as reported in previous studies [23–25]. Results show that both positive and negative defocusing can lead to a shallower and narrower weld shape due to the reduction of power density (Fig. 7 (a)). An acceptable processing window of focal position offset from −2 mm to 1 mm was therefore, determined to satisfy the joint integrity. Furthermore, similar to the thermal profile, an asymmetrical distribution of weld shape has been found where the weld is deeper and wider under negative defocusing. This phenomenon can be explained by considering the interaction of the laser beam with the molten pool surface as shown in Fig. 9. For negative defocusing (Fig. 9 (b)), when the convergent beam moves from point A to point B along the shallow surface depressed by the recoil force of evaporation, the exposure of molten surface to higher power density due to a closer position to the focused plane allows a growth of keyhole. However, this growth is restricted in the case of positive defocusing

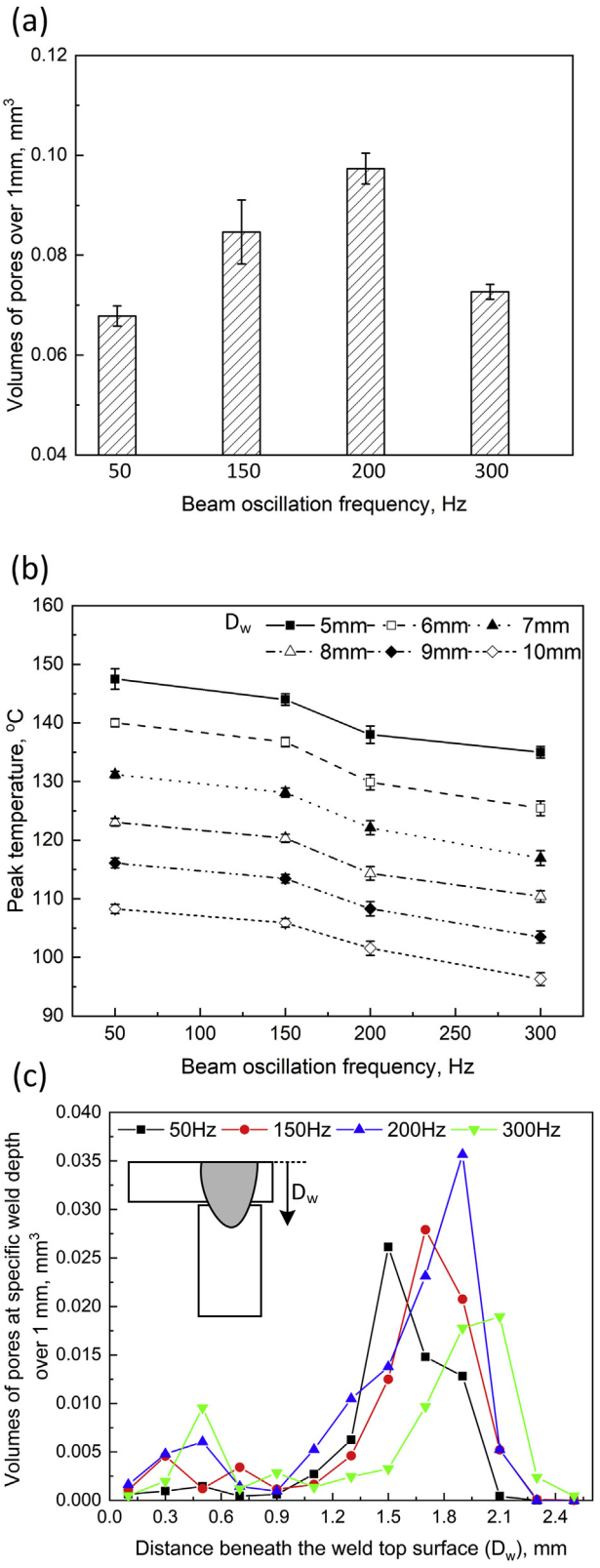

Fig. 6 – Distribution of (a) volume of pores per unit weld length (b) peak temperatures at the distance of [5 10] mm beneath the weld top surface, D_W as a function of beam oscillation frequency; and, (c) volume distribution of pores along the weld depth direction.

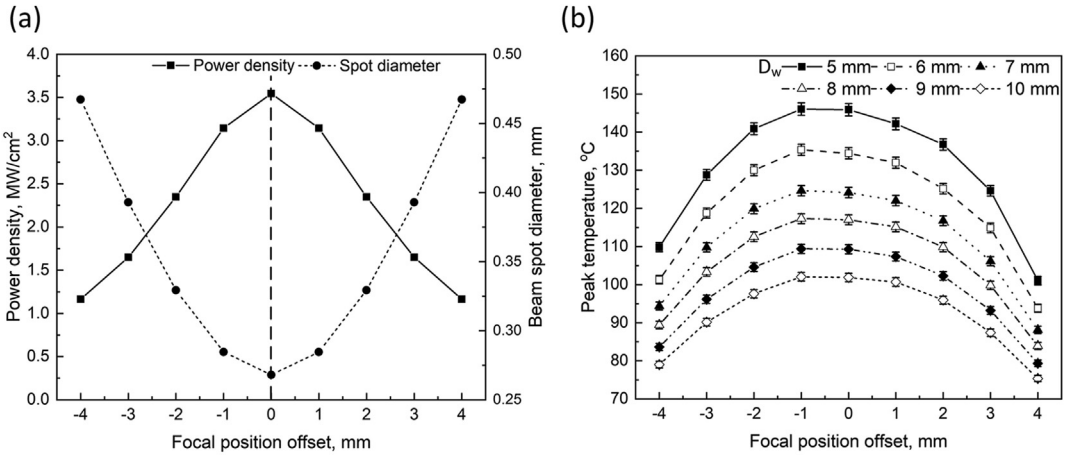

Fig. 7 – Evolution of (a) analytically computed power density and beam spot diameter on surface; and, (b) peak temperature measured on the side busbar at the distance of [5 10] mm beneath the weld top surface, D_w as function of focal position offset.

(Fig. 9 (a)) because of progressively reduced power density during the traveling of divergent laser beam from point A to Point B.

Fig. 10 visualizes the spatial distribution of pores in welds produced at different focal positions. For all welding sets, pores are predominantly located at the weld root. Fig.11 (a) quantifies the distribution of pores as a function of focal position offsets. Overall a higher positive defocusing tends to minimize the pore size at the weld root (Fig. 10) and mitigate the total volume of pores due to a lower formation rate of pores in the weld with lower weld aspect ratio (Fig.11 (b)) as confirmed by Kim et al. [26]. Furthermore, negative defocusing is more prone to weld porosity compared with positive defocusing and this can be explained by the self-stabilizing keyhole behaviour as illustrated in Fig. 9 [27]. First, beam–material interaction area increases in positive defocusing (Fig. 9 (a)) when the keyhole expands caused by any external disturbance for example, recoil pressure of vapour [28], and this can lead to the reduction of beam density which will then shrink the keyhole. Similarly, any disturbance, i.e. plasma plume [29], tends to shrink the keyhole, and thus, will exposes the keyhole to higher beam power density which will in turn, restrict the shrinkage of keyhole. Therefore, any change to the keyhole size is opposed in the case of positive

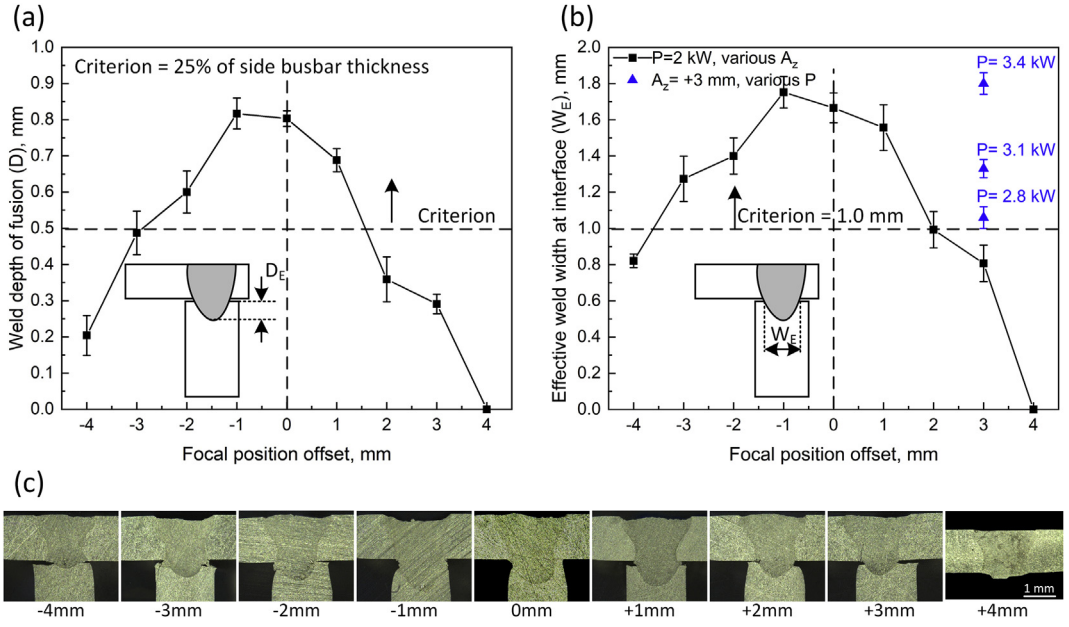

Fig. 8 – Evolution of weld shape as function of focal position offset. (a) Effective weld depth, D_E, (b) effective weld width at interface, W_E; and (c) Representative weld macro-structure. Note that (b) is overlaid with overlaid with the data obtained from welds produced at $A_z = +3$ mm with increasing power as discussed in section 3.4.

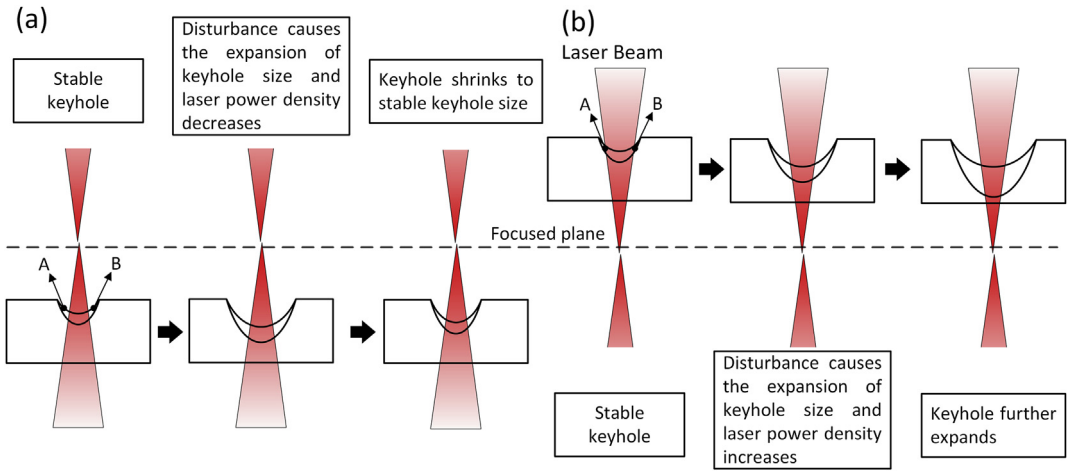

Fig. 9 – Illustration of keyhole behaviour under disturbance and interaction of laser beam with the molten surface at (a) positive and (b) negative defocusing positions [26].

defocusing and this self-stabilizing effect allows a stable keyhole behaviour. On the contrary, for negative defocusing more than 2 mm (Fig. 9 (b)), the laser focal position is beneath the bottom of the keyhole and power density increases continuously in depth. The expansion of keyhole resulting from any disturbance will cause the exposure of material in a higher power density which, in turn can further facilitate the keyhole propagation. For negative defocusing ranging from 0 to 2 mm, laser focal position is inside the weld zone and overall absorption rate within the weld zone is higher compared to the same extent of positive defocusing leading to a higher weld zone aspect ratio and hence, higher porosity formation rate [30].

3.4. *Step (II) - Effect of focal position offset on weld micro-hardness and mechanical strength*

Micro-hardness maps are shown in Fig. 12, depicting the y-z cross section, along with corresponding borders of weld zone identified from the macrographs. The base material of top busbar (AA1050-H111) and side busbar (AA1050-H14) have the hardness of 25 $Hv_{0.1}$ and 46 $Hv_{0.1}$, respectively. For 1050 aluminium alloy, it is dominantly strengthened by the plastic work during manufacturing process [31] and is therefore, a relatively higher hardness of side busbar, compared to top busbar. Overall, borders of weld zone from hardness map match reasonably with those indicated by macrograph and weld zone has a hardness between the level of two base materials. However, the deviation of focal position shows neglectable effect on the weld zone hardness. This is due to the fact that post-welding material hardness in weld zone is attributed to the grain morphology and residual strain which are mainly determined by the rapid temperature change during heating and cooling [32]. The weld speed which was reported to be a dominant factor in controlling thermal profile [33] was consistent in this study.

Tensile peel test was employed with loading along the side busbar to evaluate the effect of focal position offset on the mechanical integrity. Results plotted in Fig. 13 show a maximum joint strength at negative defocusing position of −1 mm and it corresponds to the highest bonding integrity

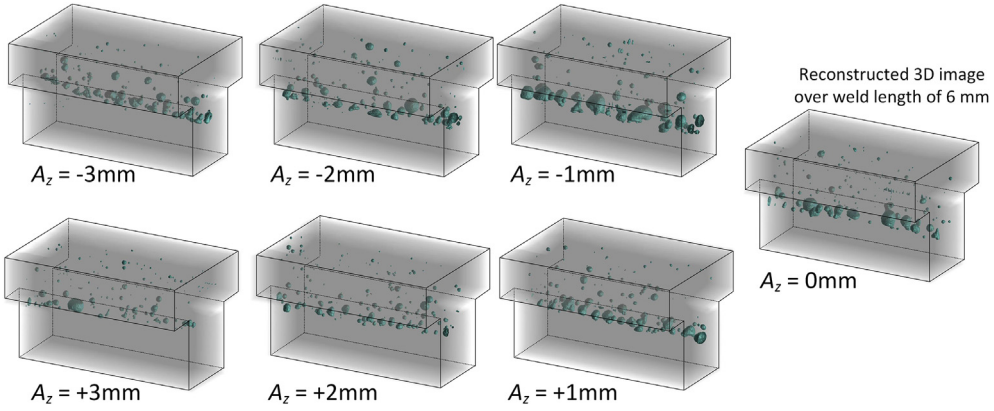

Fig. 10 – Representative 3D reconstruction of pores in welds produced with different focal positions. Note that for a better visualisation, porosity over a weld length of 6 mm was displayed.

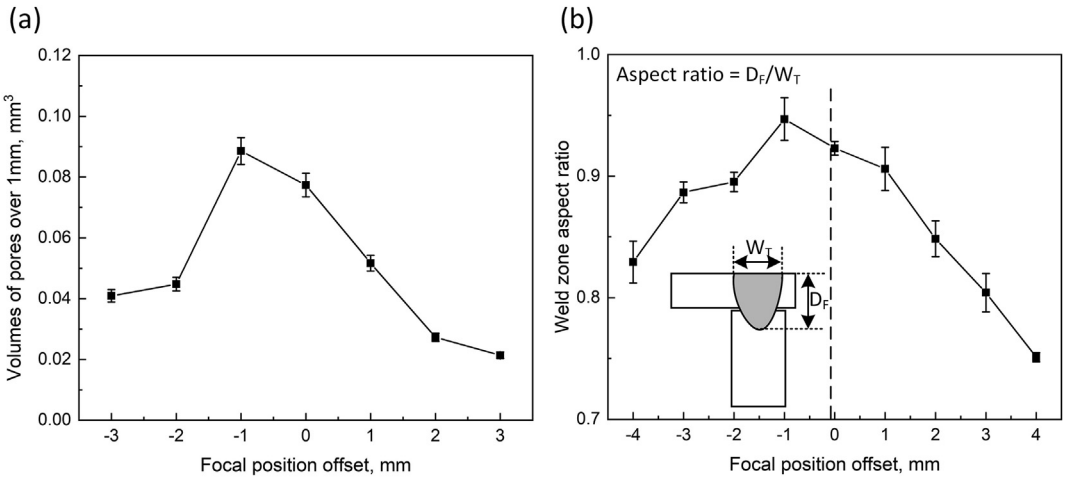

Fig. 11 – Distribution of (a) volumes of pores over 1 mm weld length and (b) weld zone aspect ratio as function of focal position offsets.

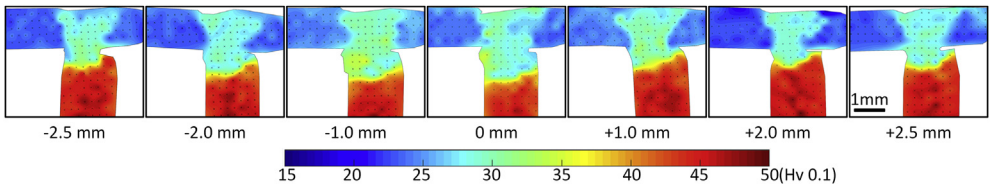

Fig. 12 – Hardness contour maps from y-z cross section of welds produced with different focal position offsets ranging from −2.5 mm to +2.5 mm the measurement grid used is indicated by the black dots and black solid lines represent the borders of the weld zone identified from the macrographs.

shown in Fig. 8. As has been indicated by the hardness distribution above, material strength within the weld zone is nearly consistent regardless of the change in focal position offsets. Therefore, joint strength is dominated by the bonding area between top busbar and side busbar, which is directly related to W_E, and weld porosity. Since a higher joint strength was observed in welds with less pores at a reduced focal offset, it is reasonable to infer that weld porosity in this paper is less effective than the effective weld width at interface, W_E on joint tensile strength. This can be further evidenced by the linear fitting between joint strength and W_E with the coefficient of determination, $R^2 = 0.94$. It should be noted that increasing the laser power can compensate the effective weld width at a higher defocusing i.e., in the case of $A_z = +3$ mm, However, the aim of this study is to investigate the effect of defocusing on the resultant weld quality regarding the effective weld width at interface and joint strength. Hence, the laser power should be consistent for a fair comparison, which otherwise can induce additional porosity as reported by Alshaer et al. [34]. In order to verify the hypotheses that weld porosity has limited impact on the joint strength, additional welding trials were conducted at $A_z = +3$ mm with the increasing laser power which in principle will increase the porosity level [34]. Results in Fig. 8 (b) and Fig. 13 (b) indicate that the improvement in the joint strength is related to the enhanced W_E and the joint strength can be reasonably fitted to the linear relationship between joint strength and W_E summarized from the welds produced at the constant power (step (II) in Table 1), thereby, confirming the limited impact of weld porosity on the joint strength in this study.

3.5. *Correlation among the weld quality properties*

Weld quality parameters such as W_E, D_E, volumes of pores and joint tensile strength are directly linked to bonding integrity and mechanical integrity. However, these quality parameters are not accessible in-line with current techniques and can only be evaluated off-line which brings challenges for in-process welding quality monitoring to meet multi-level quality requirements from the perspective of thermal, mechanical and electrical integrity in the application of busbar assembly [35]. Fig. 14 shows the positive linear correlation between in-process thermal data and off-line detectable quality parameters with $R^2 \geq 0.948$. This indicates the feasibility of in-process thermal measurement by non-contact sensors for example, IR thermal cameras and pyrometers. Further research is however necessary to address challenges related to measurement accuracy and processing time.

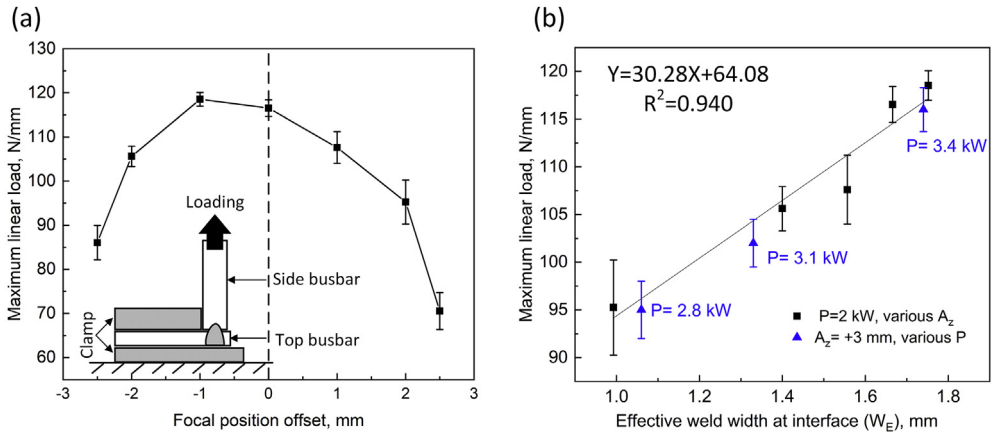

Fig. 13 – Plot of (a) maximum linear load during tensile peel test as a function of focal position offsets and (b) linear fitting between joint strength and effective weld width at interface, W_E. R^2 is the coefficient of determination for the linear fitting. Note that (b) is overlaid with overlaid with the data obtained from welds produced at $A_z = +3$ mm with increasing power as discussed in section 3.4.

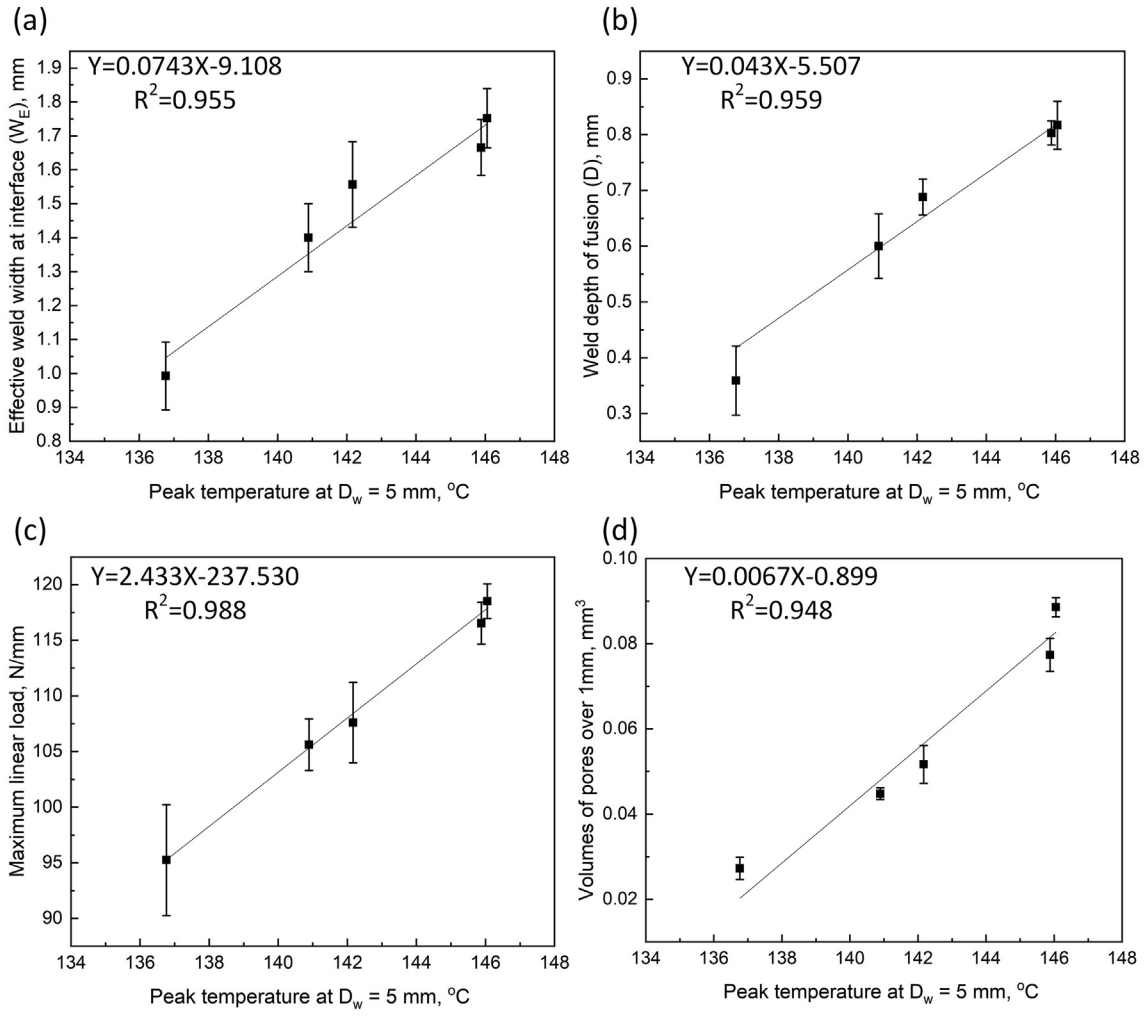

Fig. 14 – Weld quality properties as function of peak temperature determined at $D_w = 5$ mm: (a) effective weld width at interface, (b) effective weld depth, (c) maximum linear load during tensile peel test and (d) volumes of pores over 1 mm. R^2 is the coefficient of determination for the linear fitting. The higher R^2 the better the model follows the spread in the data. Note that weld quality parameters were only extracted from the processing window of focal position offset from -2 mm to 2 mm, where sufficient bonding integrity was determined.

4. Conclusions

This paper studied the effect of focal position offset on joint integrity of AA1050 battery busbar during remote laser welding. The main conclusions are summarized as follows:

(1) Defocusing of the laser beam tends to be favourable for the reduction of peak temperatures and weld porosity However, defocusing more than 3 mm can lead to 60% drop in bonding integrity which corresponds to 40% loss of joint strength.
(2) A tolerance window of focal position ranging from −2.0 mm to +1.0 mm was determined in this paper for the satisfaction of bonding integrity and mechanical integrity, which corresponds to around 70% and 30% of Rayleigh length (2.8 mm). When the accumulated variation of part tolerance, part-to-part gap and part positioning error exceeds the window of [-2, 1] mm, motorised collimator for precise focal position control is suggested.
(3) Peak temperature near weld zone shows good linear correlation with joint indicators including weld depth, weld width at interface, porosity and tensile strength. This suggests that thermal measurement can be a potential approach for the in-process monitoring of joint integrity.

Declaration of Competing Interest

The authors declare that they have no known competing financial interests or personal relationships that could have appeared to influence the work reported in this paper.

Acknowledgment

This study was financially supported by (1) WMG HVM Catapult; (2) APC UK project: ALIVE - Aluminium Intensive Vehicle Enclosures; and, (3) Innovate UK IDP15 project LIBERATE: Lightweight Innovative Battery Enclosures using Recycled Aluminium Technologies. Dr T. Sun would like to thank Mr. Paul Hadlum for the enthusiastic support at WMG Materials testing laboratory.

REFERENCES

[1] Asamer J, Graser A, Heilmann B, Ruthmair M. Sensitivity analysis for energy demand estimation of electric vehicles. Transport Res Transport Environ 2016;46:182–99. https://doi.org/10.1016/j.trd.2016.03.017.
[2] Tsiropoulos I, Tarvydas D, Lebedeva N. Li-ion batteries for mobility and stationary storage applications scenarios for costs and market growth. Publ. Off. Eur. Union Luxemb. 2018. https://doi.org/10.2760/87175. EUR 29440 EN.
[3] Lee SS, Kim TH, Hu SJ, Abell JA, Cai WW, Lee SS. Joining technologies for automotive lithium-ion battery manufacturing: a review. Int. Manuf. Sci. Eng. Conf. 2011;49460:541–9. https://doi.org/10.1115/msec2010-34168.
[4] Franciosa P, Sun T, Ceglarek D, Gerbino S, Lanzotti A. Multi-wave light technology enabling closed-loop in process quality control for automotive battery assembly with remote laser welding. Proc SPIE - Int Soc Opt Eng 2019;11059. https://doi.org/10.1117/12.2526075.
[5] Lewchalermwong N, Masomtob M, Lailuck V, Charoenphonphanich C. Material selection and assembly method of battery pack for compact electric vehicle. IOP Conf Ser Mater Sci Eng 2018;297. https://doi.org/10.1088/1757-899X/297/1/012019.
[6] Franciosa P, Serino A, Botros R Al, Ceglarek D. Closed-loop gap bridging control for remote laser welding of aluminum components based on first principle energy and mass balance. J Laser Appl 2019;31:22416. https://doi.org/10.2351/1.5096099.
[7] Ceglarek D, Colledani M, Váncza J, Kim DY, Marine C, Kogel-Hollacher M, et al. Rapid deployment of remote laser welding processes in automotive assembly systems. CIRP Ann - Manuf Technol 2015;64:389–94. https://doi.org/10.1016/j.cirp.2015.04.119.
[8] Arzanpour S, Fung J, Mills JK, Cleghorn WL. Flexible fixture design with applications to assembly of sheet metal automotive body parts. Assemb Autom 2006;26:143–53. https://doi.org/10.1108/01445150610658130.
[9] Matsunawa A, Mizutani M, Katayama S, Seto N. Porosity formation mechanism and its prevention in laser welding. Weld Int 2003;17:431–7. https://doi.org/10.1533/wint.2003.3138.
[10] Hong KM, Shin YC. Prospects of laser welding technology in the automotive industry: a review. J Mater Process Technol 2017;245:46–69. https://doi.org/10.1016/j.jmatprotec.2017.02.008.
[11] Jiang M, Chen X, Chen Y, Tao W. Mitigation of porosity defects in fiber laser welding under low vacuum. J Mater Process Technol 2020;276:116385. https://doi.org/10.1016/j.jmatprotec.2019.116385.
[12] Haboudou A, Peyre P, Vannes AB. Study of keyhole and melt pool oscillations in dual beam welding of aluminum alloys: effect on porosity formation. First Int. Symp. High-Power Laser Macroprocessing 2003;4831:295. https://doi.org/10.1117/12.503131.
[13] AlShaer AW, Li L, Mistry A. The effects of short pulse laser surface cleaning on porosity formation and reduction in laser welding of aluminium alloy for automotive component manufacture. Opt Laser Technol 2014;64:162–71. https://doi.org/10.1016/j.optlastec.2014.05.010.
[14] Wang Z, Oliveira JP, Zeng Z, Bu X, Peng B, Shao X. Laser beam oscillating welding of 5A06 aluminum alloys: microstructure, porosity and mechanical properties. Opt Laser Technol 2019;111:58–65. https://doi.org/10.1016/j.optlastec.2018.09.036.
[15] Kos M, Arko E, Kosler H, Jezeršek M. Remote laser welding with in-line adaptive 3D seam tracking. Int J Adv Manuf Technol 2019;103:4577–86. https://doi.org/10.1007/s00170-019-03875-z.
[16] Suder WJ, Williams SW. Investigation of the effects of basic laser material interaction parameters in laser welding. J Laser Appl 2012;24:32009. https://doi.org/10.2351/1.4728136.
[17] Saariluoma H, Piiroinen A, Unt A, Hakanen J, Rautava T, Salminen A. Overview of optical digital measuring challenges and technologies in laser welded components in ev battery module design and manufacturing. Batteries 2020;6:1–15. https://doi.org/10.3390/batteries6030047.
[18] ISO EN. 6892-1. Metallic materials-Tensile testing-Part 1: method of test at room temperature. Int. Organ. Stand. 2009.
[19] Fetzer F, Sommer M, Weber R, Weberpals JP, Graf T. Reduction of pores by means of laser beam oscillation during remote welding of AlMgSi. Opt Laser Eng 2018;108:68–77. https://doi.org/10.1016/j.optlaseng.2018.04.012.

[20] Zhang C, Yu Y, Chen C, Zeng X, Gao M. Suppressing porosity of a laser keyhole welded Al-6Mg alloy via beam oscillation. J Mater Process Technol 2020;278:116382. https://doi.org/10.1016/j.jmatprotec.2019.116382.
[21] Huang L, Hua X, Wu D, Fang L, Cai Y, Ye Y. Effect of magnesium content on keyhole-induced porosity formation and distribution in aluminum alloys laser welding. J Manuf Process 2018;33:43–53. https://doi.org/10.1016/j.jmapro.2018.04.023.
[22] Li S, Chen G, Zhou C. Effects of welding parameters on weld geometry during high-power laser welding of thick plate. Int J Adv Manuf Technol 2015;79:177–82. https://doi.org/10.1007/s00170-015-6813-z.
[23] Havrilla D. Successful laser welding demands optimized laser joint design. Laser Focus World 2012;48:43–8.
[24] Wu Q, Gong J, Chen G, Xu L. Research on laser welding of vehicle body. Opt Laser Technol 2008;40:420–6. https://doi.org/10.1016/j.optlastec.2007.06.004.
[25] Sinha AK, Kim DY, Ceglarek D. Correlation analysis of the variation of weld seam and tensile strength in laser welding of galvanized steel. Opt Laser Eng 2013;51:1143–52. https://doi.org/10.1016/j.optlaseng.2013.04.012.
[26] Kim JS, Watanabe T, Yoshida Y. Effect of the beam-defocusing characteristics on porosity formation in laser welding. J Mater Sci Lett 1995;14:1624–6. https://doi.org/10.1007/BF00455435.
[27] Pastor M, Zhao H, Martukanitz RP, Debroy T. Porosity, underfill and magnesium loss during continuous wave Nd:YAG laser welding of thin plates of aluminum alloys 5182 and 5754. Weld J (Miami, Fla) 1999;78:207–s.
[28] Qiu W, Yang L, Zhao S, Yang R, Liu T. A study on plasma plume fluctuation characteristic during A304 stainless steel laser welding. J Manuf Process 2018;33:1–9. https://doi.org/10.1016/j.jmapro.2018.04.001.
[29] Wael A, Shaer A. Porosity reduction and elimination in laser welding of aa6014 aluminium alloys for automotive components manufacture and industrial applications. The University of Manchester (United Kingdom); 2017.
[30] Lin R, Wang H ping, Lu F, Solomon J, Carlson BE. Numerical study of keyhole dynamics and keyhole-induced porosity formation in remote laser welding of Al alloys. Int J Heat Mass Tran 2017;108:244–56. https://doi.org/10.1016/j.ijheatmasstransfer.2016.12.019.
[31] Association A.. Aluminum: properties and physical metallurgy. ASM international; 1984.
[32] Moraitis GA, Labeas GN. Residual stress and distortion calculation of laser beam welding for aluminum lap joints. J Mater Process Technol 2008;198:260–9. https://doi.org/10.1016/j.jmatprotec.2007.07.013.
[33] Cao X, Wallace W, Immarigeon J-P, Poon C. Research and progress in laser welding of wrought aluminum alloys. Ii. Metallurgical microstructures, defects, and mechanical properties. Mater Manuf Process 2003;18:23–49. https://doi.org/10.1081/AMP-120017587.
[34] Alshaer AW, Li L, Mistry A. Understanding the effect of heat input and sheet gap on porosity formation in fillet edge and flange couch laser welding of AC-170PX aluminum alloy for automotive component manufacture. J. Manuf. Sci. Eng. Trans. ASME 2015;137:1–13. https://doi.org/10.1115/1.4028900.
[35] Zwicker MFR, Moghadam M, Zhang W, Nielsen CV. Automotive battery pack manufacturing – a review of battery to tab. J. Adv. Join. Process 2020;1:100017. https://doi.org/10.1016/j.jajp.2020.100017.